Properties of the iron-sulfur cluster electron transfer relay in an [FeFe]-hydrogenase that is tuned for H_2 oxidation catalysis

Received for publication, February 12, 2024, and in revised form, April 9, 2024 Published, Papers in Press, April 16, 2024,
https://doi.org/10.1016/j.jbc.2024.107292

Effie C. Kisgeropoulos[1], Jacob H. Artz[1], Matthew Blahut[1], John W. Peters[2], Paul W. King[1,3], and David W. Mulder[1,*]

From the [1]Biosciences Center, National Renewable Energy Laboratory, Golden, Colorado, USA; [2]Department of Chemistry and Biochemistry, The University of Oklahoma, Norman, Oklahoma, USA; [3]Renewable and Sustainable Energy Institute, National Renewable Energy Laboratory and University of Colorado Boulder, Boulder, Colorado, USA

Reviewed by members of the JBC Editorial Board. Edited by Joan B. Broderick

[FeFe]-hydrogenases catalyze the reversible oxidation of H_2 from electrons and protons at an organometallic active site cofactor named the H-cluster. In addition to the H-cluster, most [FeFe]-hydrogenases possess accessory FeS cluster (F-cluster) relays that function in mediating electron transfer with catalysis. There is significant variation in the structural properties of F-cluster relays among the [FeFe]-hydrogenases; however, it is unknown how this variation relates to the electronic and thermodynamic properties, and thus the electron transfer properties, of enzymes. *Clostridium pasteurianum* [FeFe]-hydrogenase II (CpII) exhibits a large catalytic bias for H_2 oxidation (compared to H_2 production), making it a notable system for examining if F-cluster properties contribute to the overall function and efficiency of the enzyme. By applying a combination of multifrequency and potentiometric electron paramagnetic resonance, we resolved two electron paramagnetic resonance signals with distinct power- and temperature-dependent properties at g = 2.058 1.931 1.891 ($F_{2.058}$) and g = 2.061 1.920 1.887 ($F_{2.061}$), with assigned midpoint potentials of −140 ± 18 mV and −406 ± 12 mV *versus* normal hydrogen electrode, respectively. Spectral analysis revealed features consistent with spin-spin coupling between the two [4Fe-4S] F-clusters, and possible functional models are discussed that account for the contribution of coupling to the electron transfer landscape. The results signify the interplay of electronic coupling and free energy properties and parameters of the FeS clusters to the electron transfer mechanism through the relay and provide new insight as to how relays functionally complement the catalytic directionality of active sites to achieve highly efficient catalysis.

Electron transfer is critical to the function of enzymatic oxidation-reduction reactions for biological energy conversion and is mediated by organic and inorganic redox active cofactors, including iron-sulfur (FeS) clusters (1–3). FeS clusters differ in composition and display a wide range of reduction potentials and electronic properties that can support the diverse electron transfer requirements found in redox catalysis, including critical energy transformation reactions such as reversible H_2 oxidation, N_2 fixation, and CO_2 reduction (4–6). Another superfamily of FeS cluster enzymes termed radical *S*-adenosylmethionine (SAM) enzymes catalyze a diverse array of radical based reactions by means of a site-differentiated [4Fe-4S]-SAM complex (7–9). Fine-tuning of FeS cluster properties in proteins (reviewed in (10)) is possible through modification of primary coordination (*e.g.*, cysteine, serine, and histidine amino acid ligation) (11–14), secondary and outer sphere coordination (*e.g.* H-bonding, electrostatics, and electric fields) and solvation (15–18). Magnetic dipolar and exchange interactions are also possible *via* spin-spin coupling between FeS clusters or with other nearby paramagnetic species, such as flavin semiquinones (19, 20). In total, the highly tunable nature and modular architecture of FeS clusters make them ideally suited as components of biological redox relays that function in electron transfer (21). This is exemplified by the wide distribution of FeS cluster relays in biological systems, such as those found in respiratory and photosynthetic electron transport chains (22, 23), and redox enzymes such as [NiFe]-hydrogenases (24–26), [FeFe]-hydrogenases (27–29), sulfite reductase (25), carbon monoxide dehydrogenase (30), formate dehydrogenase (31), and nitrogenase (32).

For FeS cluster relays found in redox enzymes, the relay carries out the essential role of mediating the exchange of electrons between the active site, where substrate reduction or oxidation occurs, and external donor-acceptor molecules (*e.g.* ferredoxin). The rate and the directional specificity of electron-transfer (*i.e.* ratio of forward and reverse rates) through relays are important factors for the efficient coupling of electron transfer to catalysis (33, 34). This is due to the fast turnover as well as the biased nature of the redox reactions, which can occur at a different rate in one direction (*e.g.* reduction) *versus* the reverse direction (*e.g.* oxidation) (35–37). Marcus theory

$$k_{ET} = \frac{2\pi}{\hbar} \frac{|H_{AB}|^2}{\sqrt{4\pi\lambda k_B T}} \exp\left[-\frac{(\Delta G^\circ + \lambda)^2}{4\lambda k_B T}\right] \quad (1)$$

provides a framework for understanding the parameters that contribute to the control of kinetic rates of electron transfer (k_{ET}), including its dependence on free energy (ΔG), reorganization energy (λ), and electronic coupling $|H_{AB}|^2$

* For correspondence: David W. Mulder, David.Mulder@nrel.gov.

(Equation 1) (38, 39). For relays consisting of multiple FeS clusters, spaced within distances to allow for fast electron transfer (2), the exchange interaction (J) arising from spin-spin coupling between nearby clusters is fundamentally linked to the electronic coupling parameter, $|H_{AB}|^2$ (40–42). The optimization of Marcus parameters, for example, through the arrangement of FeS clusters or tuning mechanisms by the protein environment, is important for controlling rates of electron transfer and the efficiency of long-range tunneling mechanisms (2, 43–45). Marcus theory is limited, however, in describing how underlying cofactor properties and interactions, such as coupling within relays or the density of spin-states of the FeS clusters that comprise relays, influence electron transfer rates. More specifically, there are outstanding questions regarding the collective influence of the underlying properties of relays beyond reduction potentials on directional electron transfer kinetics, which can be defined as the difference in forward *versus* reverse rates of electron transfer. Determining this is important for understanding how FeS cluster relays contribute to the efficiency and high rates of catalysis observed for redox enzymes.

[FeFe]-hydrogenases catalyze the reversible oxidation of H_2 from protons and electrons ($2H^+ + 2e^- \leftrightarrows H_2$) through a unique catalytic cofactor active-site termed the H-cluster (46). For the majority of [FeFe]-hydrogenases, the exchange of electrons that happens during H_2 catalysis between the active site H-cluster and physiological redox partner, for example, ferredoxin (Fdx), is achieved and mediated *via* a network of FeS clusters, referred to as F-clusters. F-clusters, which most commonly exist as [4Fe-4S] and [2Fe-2S] ferredoxin-type domains (47, 48), form electron relays, analogous to electrical wires, between the H-cluster and Fdx. Examination of [FeFe]-hydrogenase structures (27–29) show that F-clusters are typically found in spatial arrangements where the distance between individual clusters (~8–12 Å) is within the boundary for high tunneling rates (2) and collectively facilitate fast electron transfer across large distances. Given the significant variation in the structural complexity of F-cluster domains among the [FeFe]-hydrogenases, including the number, type, and spatial arrangement of FeS clusters, it is interesting to examine how underlying properties of the relay allow for the efficient coupling of long-range electron transfer to reversible H_2 oxidation.

It has been shown that the absence or presence of F-cluster domains can alter the H_2 evolution activity in [FeFe]-hydrogenases such as HydA from *Clostridium acetobutylicum* (CaI) (49, 50) and HydA from *Megasphaera elsdenii* (51), demonstrating that F-clusters can influence the overall efficiency of the reaction. For the CaI F-cluster relay in particular, ligand modification of a site-differentiated [4Fe-4S] cluster that serves as the entry/exit point for electrons was shown to alter the electronic-spin properties of the cluster and resulted in an attenuation for H_2 production and H_2 oxidation activities (12). These observations suggest that properties of relays can affect the catalytic reactivity of the enzyme. They also raise questions as to whether underlying properties and interactions within relays, such as electronic coupling between FeS clusters, have evolved to functionally complement or directionally match relay electron transfer kinetics to the catalytic bias observed at the active site H-cluster.

The [FeFe]-hydrogenase II from *Clostridium pasteurianum* (CpII) functions under nitrogen-fixing conditions to oxidize H_2 to recycle reduced Fdx (52). It is highly adapted for this role by having a large bias toward H_2 oxidation catalysis (53–55) (Fig. 1). The H_2 oxidation bias of CpII is unique compared to other [FeFe]-hydrogenases, making it an interesting case for examining if properties of the relay function to support the overall efficiency of the catalytic reaction. The relay of CpII as shown in Figure 1 (and Fig. S1) consists of two [4Fe-4S] F-clusters that, along with the H-cluster and the Fdx [4Fe-4S] clusters, form a wire of clusters spaced roughly equidistant from each other. H_2 production assays using reduced Fdx as an electron donor, which donates electrons into the relay, show different rates of H_2 production for CpII *versus* the [FeFe]-hydrogenase I from *C. pasteurianum* (CpI) (53, 54). Likewise, electrochemical studies of CpII and CpI absorbed onto an electrode, a setup that would presumably mimic the Fdx as a donor acceptor, show clear differences in the profiles of cyclic voltammograms, with CpII favoring H_2 oxidation over H_2 production (53). These observations suggest there are differences in the relays that determine or tune directionally specific rates of electron transfer through the relay. For CpII, this is hypothesized here to support faster kinetics for flow away from the H-cluster (Fig. 1, bold arrows) *versus* flow to the H-cluster (Fig. 1, dotted arrows), to match to the catalytic directionality and bias for the H_2 oxidation reaction.

Previous characterization of CpII by Adams and others demonstrated that one of the [4Fe-4S] clusters of the F-cluster relay has an unusually high midpoint potential (E_m = −180 mV), while the other [4Fe-4S] cluster E_m was only estimated at < −300 mV (56) due to unresolved complexity of overlapping signals. Whereas the −180 mV potential has been modeled to the [4Fe-4S] cluster that is distal in relation to the H-cluster (55, 57), an assignment to the [4Fe-4S] cluster proximal the H-cluster is also possible, with support for either configuration lacking direct experimental evidence. An issue with the previously proposed model assigning the distal cluster E_m as −180 mV is that it creates a large endergonic barrier for the transfer of electrons to Fdx, which has previously been determined to have an E_m = −412 mV (58). Such a barrier would likely result in slow electron transfer kinetics for Fdx reduction that do not match the high rates of H_2 oxidation reactivity from biochemical assays (53–55). The difficulty in rationalizing how a relay created from disparate E_m values is able to support fast and efficient electron transfer for coupling of the H_2 oxidation reaction to reduction of the Fdx redox partner suggests that factors other than free-energy alone might contribute to the tuning of electron transfer rates through the CpII relay. Of particular interest is the possible magnetic interaction between the two [4Fe-4S] F-clusters that would be anticipated due to the short distance and intervening protein structure between the two F-clusters.

In this work, the electronic and thermodynamic properties of the CpII F-clusters were determined to decipher if the

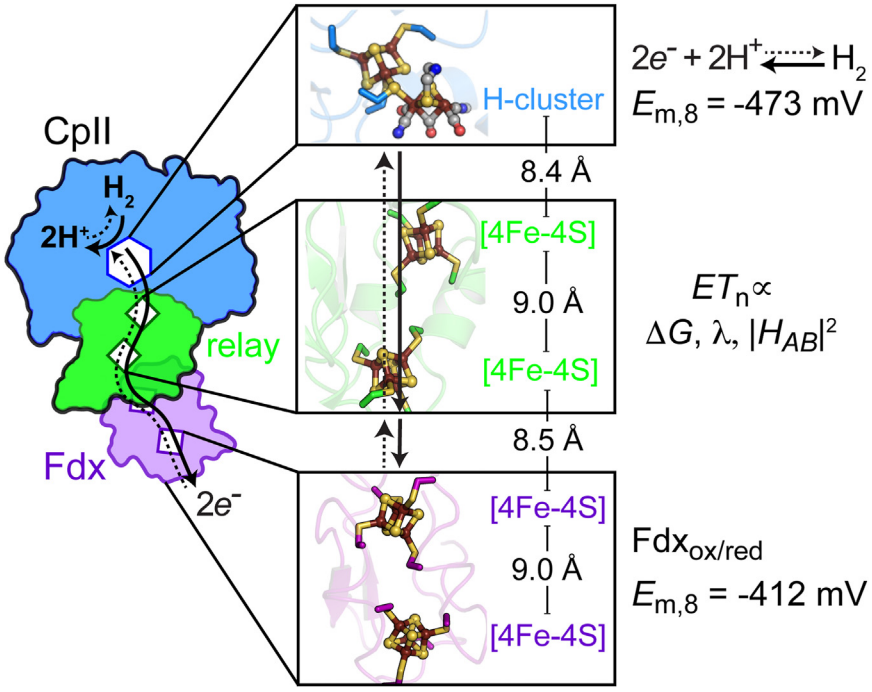

Figure 1. Cartoon model of the [FeFe]-hydrogenase CpII-ferredoxin (Fdx) complex from *Clostridium pasteurianum* based on the predicted AlphaFill/AlphaFold structural model (Fig. S1). The *zoomed regions* depict the CpII two [4Fe-4S] F-cluster relay which mediates electron transfer between the active site H-cluster and external Fdx during reversible H_2 oxidation catalysis (edge to edge cluster distances labeled in Angstroms, Å). $E_{m,8}$ refers to the respective midpoint potentials at pH 8 of the H^+/H_2 electrode and the oxidized/reduced [4Fe-4S] Fdx couple ($Fdx_{ox/red}$) (58). The rate of electron transfer (ET_n) is dependent on free energy (ΔG), reorganization energy (λ), and electronic coupling ($|H_{AB}|^2$) Marcus parameters. CpII, *Clostridium pasteurianum* [FeFe]-hydrogenase II; Fdx, ferredoxin.

electron relay found in CpII is tuned to contribute to the efficiency of the overall reaction that is strongly biased for H_2 oxidation catalysis. Using multifrequency, CW X-band (9.8 GHz) and pulsed Q-band (33.8 GHz), we assigned the electron paramagnetic resonance (EPR) signals and identified magnetic interactions within the relay that originate from spin-spin coupling between the two [4Fe-4S] F-clusters. With this information resolved, the midpoint potential values were obtained for both clusters by potentiometric EPR. These properties were used to evaluate models for mapping the F-cluster potentials onto the spatial organization of the F-clusters in the CpII structure. From this analysis, a mechanism based on the framework of Marcus theory is proposed that accounts for how the relay is tuned to facilitate directionally specific electron transfer during H_2 oxidation catalysis. The design principles elucidated here for CpII are discussed in the context of tuning the directionality of reduction-oxidation reaction chemistry in other redox enzymes where certain bias has been observed or is a desired property.

Results

Resolution of the F-cluster EPR signatures in CpII reveal a spin-coupled relay

To decipher the F-cluster relays properties of CpII, we utilized variable-temperature, variable-power CW X-band and temperature-dependent pulsed Q-band EPR. This approach provided a strategy for overcoming the lack of resolution between overlapping EPR signals of the two [4Fe-4S] F-clusters by leveraging differences in the cluster relaxation properties to resolve signal contributions. The multilayered dataset was complimented by a spectral simulation analysis to further validate the spectroscopic assignments. In line with previous reports (54–56), the CW X-band spectra of H_2 reduced CpII collected at 15 to 24 K displayed a near uniform rhombic signal of g = 2.058, 1.931, and 1.891 (referred to here as $F_{2.058}$) which can be assigned to one of the reduced S = ½ $[4Fe\text{-}4S]^{1+}$ F-clusters (Figs. 2*A* and S2). At temperatures below 15 K, a faster relaxing signal could be resolved with the aid of Q-band data (discussed in detail below) at g = 2.061, 1.920, and 1.887 (referred to here as $F_{2.061}$) and assigned to the other reduced S = ½ $[4Fe\text{-}4S]^{1+}$ F-cluster. The resolution of the signal is signified by shifting of the peak at $g \sim 2.058$ to $g \sim 2.061$ (Fig. 2*A*, inset), concomitant with increased signal intensity at $g \sim 1.9$ as the collection temperature was lowered. The spectra also became more complex at lower temperatures in a manner indicative of spin-spin coupling between two S = ½ $[4Fe\text{-}4S]^{1+}$ clusters. This included appearance of a feature centered at $g \sim 2.015$ and anisotropic broadening of the overall signal. It is noted that the observed signals are not thought to arise from other possible reduced paramagnetic H-cluster states such as H_{sred} and H_{hyd} (59, 60), as distinguishing EPR features from these signals were not readily identified in the spectra. Spectral broadening on the wings could indicate some presence of H_{sred}; however, other prominent features of H_{sred} at g = 2.145 and 1.860 as characterized from the HydA1 [FeFe]-

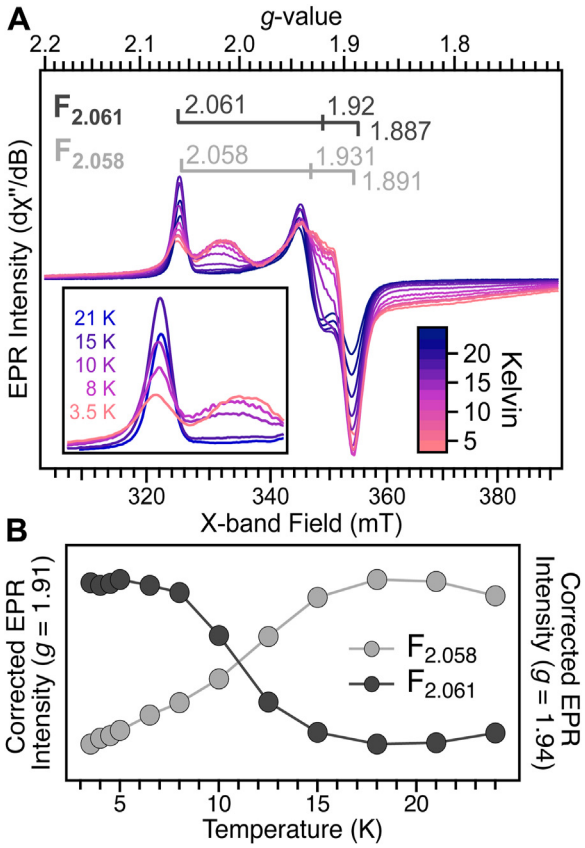

Figure 2. EPR properties of the reduced F-clusters of CpII. *A*, variable temperature, CW X-band EPR spectra of 100% H_2 reduced CpII. Data collected at 1 mW and shown prior to correction for the Curie law. The inset shows the magnification of the g_1 turning point and the center of the peak which shifts with temperature. *B*, Curie plot showing the temperature-dependent behavior of $F_{2.058}$ and $F_{2.061}$ signals. EPR intensities at g = 1.94 ($F_{2.058}$) or g = 1.91 ($F_{2.061}$) were obtained from 1 mW data shown in (*A*) and corrected for a Curie law dependence by multiplication of the intensity by the collection temperature; flat regions indicate no temperature saturation effects. CpII, *Clostridium pasteurianum* [FeFe]-hydrogenase II; EPR, electron paramagnetic resonance; $F_{2.058}$, F-cluster signal designated at g = 2.058, 1.931, 1.891; $F_{2.061}$, F-cluster signal designated at g = 2.061, 1.920, 1.887.

hydrogenase from *Chlamydomonas reinhardtii* (CrHydA1) (60) were not identified in the reduced EPR spectra of CpII.

Analysis of the temperature- and power-dependent spectral behavior supports the distinct nature of the $F_{2.058}$ and $F_{2.061}$ signals (Table S1). Notably the two signals displayed different temperature optima (T_{opt}) and opposite temperature-dependent trends (Figs. 2*B* and S3). The $F_{2.058}$ signal increased in intensity with temperature up to 18 K and began to decrease at 24 K (T_{opt} = 18–21 K at 1 mW). On the other hand, the $F_{2.061}$ signal maximized at lower temperatures with evidence of temperature saturation only at the lowest collection temperature (T_{opt} = 3.5–6.5 K at 1 mW). The power saturation behavior of the two signals was also distinct (Fig. S4), with a lower power optimum (P_{opt}) for $F_{2.058}$ (P_{opt} = 0.01–0.1 mW) compared to $F_{2.061}$ (P_{opt} = 1–20 mW) at 10 K, where temperature saturation effects on the spectra were minimized for both species. The feature at g = 2.015 had a temperature and power response close to that of $F_{2.061}$ and likewise was very distinct from $F_{2.058}$.

To further resolve the two F-cluster signals and assess possible signals due to spin-spin coupling between the clusters, pulsed Q-band EPR spectra of H_2-reduced CpII were collected at temperatures between 8.8 and 14.4 K (Figs. 3, S5 and S6). Similar to the X-band data, the $F_{2.058}$ species was the dominant signal at higher temperature (14.4 K) with distinct spectral shifts consistent with the $F_{2.061}$ species observed as temperature was lowered to 8.8 K (Fig. 3*A*). Namely, the low-field edge of the absorption envelope near $g \sim 2.06$ became more asymmetric in the pseudomodulated spectra, and the absorption peak maximum near g = 1.93 shifted toward g = 1.92. The feature at g = 2.015 was also less pronounced in the Q-band data, along with other features of the $F_{2.061}$ signal. This was supported by a sweep of the pulse EPR parameters (Fig. S5), which indicated faster-relaxing spin-packet(s) associated with both the $F_{2.061}$ signal and g = 2.015 feature compared to that of the $F_{2.058}$ signal.

Multifrequency, global simulations of the X- and Q-band data using EasySpin (61) verified the $F_{2.058}$ and $F_{2.061}$ signal assignments (Figs. 3, S6, and Table S2). The $F_{2.058}$ signal was initially resolved from the multifrequency fitting of 14.4 K (Q-band) and 21 K (X-band) data (Fig. S6). This made possible an ensuing global simulation of the 8.8 K (Q-band) and 10 K (X-band) data, which resolved the $F_{2.061}$ signal and resulted in a high-quality simulation of the Q-band data (Figs. 3*A* and S6). The Q-band simulation displayed excellent agreement with the spectral breadth and major turning points of the experimental spectra, while the X-band simulation also reproduced these aspects but did not account for the spectral feature at g = 2.015 and, to an extent, broadening (Fig. S6). Overall, the weaker intensity of the g = 2.015 feature and diminished broadening of the spectra in the Q-band data resulted in better simulations at Q-band compared to X-band. Spectral features arising from spin-spin coupling are defined by magnetic field-independent terms in the spin Hamiltonian, and as a consequence can appear to have less impact on the spectral shape as magnetic field increases (*i.e.*, from X-band to Q-band) (62, 63). This is in line with the greater disparity observed between the X-band experimental data and simulations, specifically.

To further evaluate the contribution of spin-spin coupling to the data, the line shapes of X- and Q-band spectra were examined (Fig. 3*B*). As described above, spectral contributions from spin-spin coupling do not scale with field; therefore, when multifrequency data are plotted on an equivalent g-value scale, such features are expected to appear narrower in spectra collected at higher frequency (20, 63, 64). When compared to X-band data collected at similar temperatures, the Q-band spectrum was significantly narrower on the lower field ($g \sim$ 2.06) side of the absorption profile, and slightly narrower at the higher field ($g \sim$ 1.89) edge. The feature at g = 2.015 was also narrower at Q-band, although this was less pronounced due to the lower signal intensity (Fig. 3*B*, inset). Overall, the narrowing effects observed between the two microwave frequencies are consistent with spectral contributions arising from spin-spin coupling between the two [4Fe-4S] F-clusters. From a structural perspective, spin-spin coupling between the

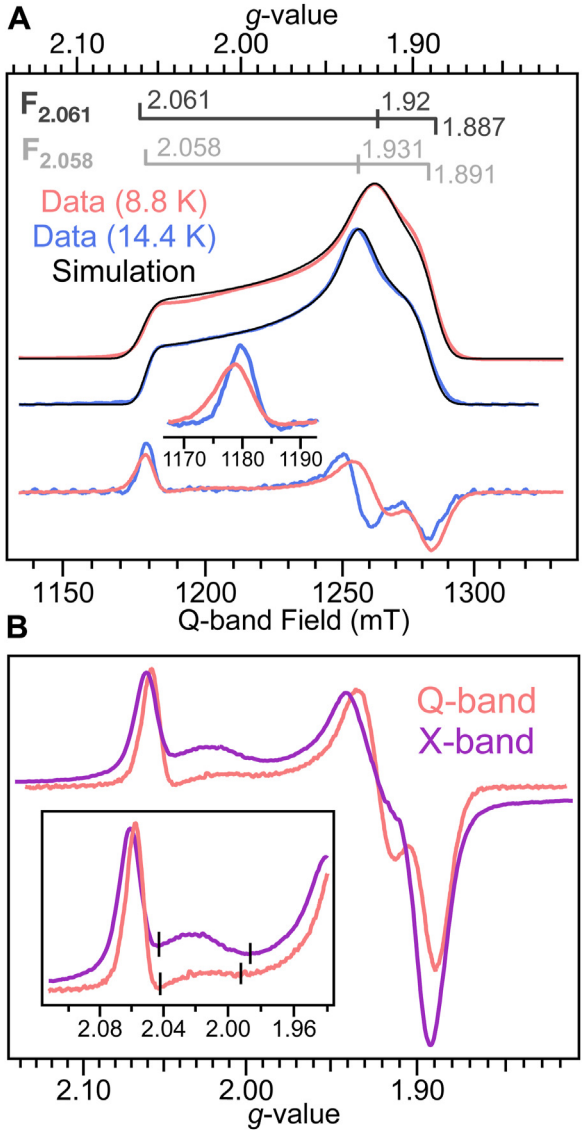

Figure 3. Multifrequency EPR analysis of reduced CpII. *A*, pulsed Q-band EPR spectra of H_2 reduced CpII collected at 8.8 K (*pink*) or 14.4 K (*blue*). *Top*, absorbance data are shown offset from one another with simulations overlaid in *black*; the data at 14.4 K is simulated using only the $F_{2.058}$ species while the 8.8 K simulation includes contribution from both $F_{2.058}$ and $F_{2.061}$ (Table S2). *Bottom*, pulse Q-band data shown overlaid after applying pseudomodulation, with inset highlighting the temperature-dependent change in peak shape. *B*, overlay of CW X-band (10 K) and pulse Q-band (8.8 K) experimental data, normalized to the signal peak at $g \sim 2.06$. The inset shows narrowing in the line width of the $g = 2.015$ feature going from X-to Q-band, consistent with it originating from spin-spin coupling between the two [4Fe-4S] F-clusters. CpII, *Clostridium pasteurianum* [FeFe]-hydrogenase II; EPR, electron paramagnetic resonance; $F_{2.058}$, F-cluster signal designated at $g = 2.058$, 1.931, 1.891; $F_{2.061}$, F-cluster signal designated at $g = 2.061$, 1.920, 1.887.

two clusters would be expected. The AlphaFill model generated from the AlphaFold structure of CpII (Figs. 1 and S1) shows that the two [4Fe-4S] clusters are separated by 9.0 Å, well within distances at which these couplings can occur. We also note that similar spin-spin coupling signals have been observed for other two [4Fe-4S] cluster containing systems including Fdxs (65–68), other [FeFe]- and [NiFe]-hydrogenases (64, 69–72), and the PsaC subunit of the photosynthetic I electron transport chain (73, 74).

Redox landscape of the CpII F-clusters

With the spectral properties of $F_{2.058}$ and $F_{2.061}$ resolved, potentiometric EPR studies were performed to determine the reduction potentials of the two [4Fe-4S] clusters and the degree of spin-spin coupling as function of potential. CpII was subjected to a redox titration using a cocktail of mediators and sodium dithionite (NaDT) to modulate the solution potential with continuous equilibration. Five samples of redox poised CpII were prepared in this manner, spanning potentials from −129 mV to −493 mV *versus* normal hydrogen electrode (NHE). Using the diverging spin relaxation behavior of the [4Fe-4S] clusters (Table S1), EPR spectra of potentiometric samples were collected at 3.7 K (Fig. 4) and 20 K (Fig. S7) to assess the midpoint potentials of the $F_{2.061}$ and $F_{2.058}$ species, respectively. For both collection temperatures, signal from the oxidized H-cluster state (H_{ox}) at $g = 2.080$, 2.028, and 2.000 was observed (56), as well as an isotropic signal at $g \sim 2.001$, which is attributed to radical species from redox mediators (Table S2). Additionally, a shoulder at $g \sim 2.088$ was observed in samples containing H_{ox} contribution (Figs. 4 and S7), which is thought to correspond to a second H_{ox} signal that slightly shifts with pH, as previously described (56).

Fitting and simulation of the potentiometric EPR data provided an overall signal intensity (defined as the simulated system weight in EasySpin) for each species at each potential (Table S2). These intensities were subsequently plotted *versus* the solution potential for $F_{2.061}$ and $F_{2.058}$ and fit to the n = 1 Nernst equation to determine approximate E_m values (see Experimental procedures). It is noted that the $F_{2.061}$ signal in the g ∼ 1.9 region did not clearly grow in until −395 mV (Fig. 4) and continued to increase in the lowest potential data of the titration (−493 mV). For all potentials, the overlapping (and temperature-saturated) signal of $F_{2.058}$ hindered a more perfect simulation of the line shape of the 3.7 K spectra. With these factors considered, a high-quality Nernst fit was still obtained with a rise and slope which overlaid the experimental data with excellent agreement. The results gave an E_m value of −406 mV ± 12 *versus* NHE for $F_{2.061}$ (Fig. 4, inset). Using the same approach with data collected at 20 K (Fig. S7), the results gave an E_m value of −140 ± 18 mV *versus* NHE for $F_{2.058}$ (Fig. 4, inset). The slight difference compared to the previously reported value of −180 mV for the signal (56) can be attributed to the higher temperature used here to analyze the signal response (20 K *versus* 15 K), which was necessary to completely avoid temperature saturation of the $F_{2.058}$ signal at a microwave power of 1 mW (Table S1). In addition to the [4Fe-4S] F-cluster signals, the potentiometric data showed that the $g = 2.015$ coupling signal increased in intensity from −395 mV to −493 mV. This occurred alongside the appearance of the $F_{2.061}$ signal, consistent with the origin of the $g = 2.015$ signal from spin-spin coupling between the two reduced $[4Fe\text{-}4S]^{1+}$ F-clusters.

In performing simulations of the potentiometric data shown in Figure 4 and Fig. S7, small shifts in the $F_{2.058}$ and $F_{2.061}$ spin-Hamiltonian parameters were required to obtain the best fits (Table S2). This was most pronounced around the g_1 and g_2 regions and was observed even in the higher potential

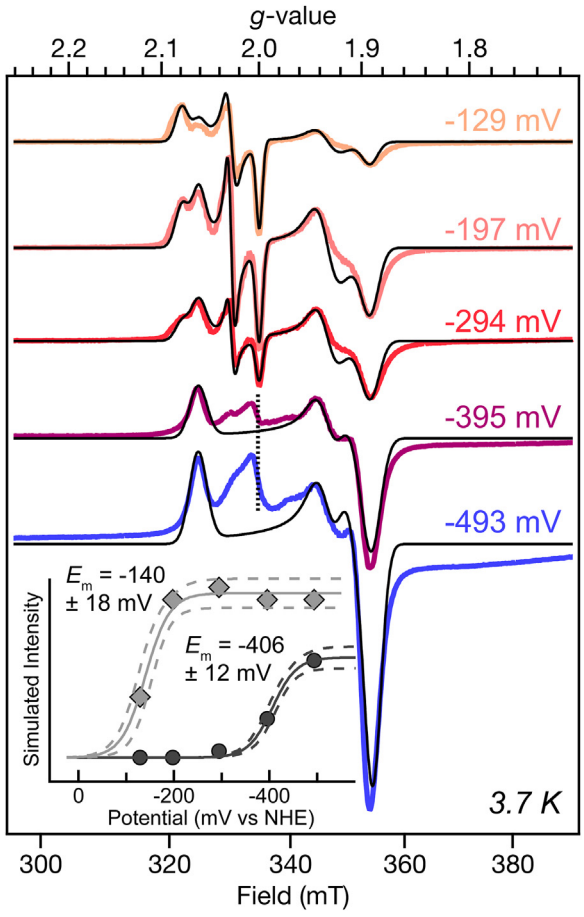

Figure 4. Potentiometric EPR data and analysis of CpII. Simulations are overlaid (*black lines*) and were performed using varying contributions from H_{ox}, $F_{2.058}$, and $F_{2.061}$ (Table S2). At potentials negative of −294 mV, a radical signal originating from redox mediators is indicated with a *dotted line*. *Inset*, the simulated total signal intensities of $F_{2.061}$ (•) and $F_{2.058}$ (◆) (Table S2), obtained from simulation of 3.7 K or 20 K (Fig. S7) data, respectively, and plotted as a function of potential. Data were fit to the Nernst equation (*solid lines*) to obtain E_m values, with the 95% confidence bands of each model shown as *dashed lines* and error reported as the ±95% confidence interval. See Experimental procedures for further details. CpII, *Clostridium pasteurianum* [FeFe]-hydrogenase II; E_m, midpoint potential; EPR, electron paramagnetic resonance; $F_{2.058}$, F-cluster signal designated at g = 2.058, 1.931, 1.891; $F_{2.061}$, F-cluster signal designated at g = 2.061, 1.920, 1.887.

(*e.g.*, −197 mV) data collected at 20 K, where the only spectral contributions are from the paramagnetic H_{ox} species of the H-cluster and $F_{2.058}$. These observations are consistent with previous EPR of CpII, which also displayed small shifts in *g*-value of one of the F-clusters signals (g = 2.06 1.93 1.90) depending on the reduction method (55, 56). Using the spin-Hamiltonian parameters determined from the potentiometric data to re-simulate the 100% H_2 reduced Q-band data did not result in an improved fit, suggesting the presence of additional magnetic phenomena in the potentiometric data. This can be explained by the presence of H_{ox}, since H_{ox} was not observed in the H_2 reduced sample examined above. Given that the H-cluster in H_{ox} is an effective S = ½ species and located within ∼8.5 Å of the proximal F-cluster (Figs. 1 and S1), it is plausible that spin-spin coupling between the two clusters could modulate the apparent *g*-values of the signals. Indeed, magnetically interacting [4Fe-4S] clusters can give rise to shifts in observed *g*-values in potentiometric titrations (19, 75).

Discussion

FeS cluster relays comprise an integral component of redox enzymes for linking electron transfer with catalytic reactions and energy transformation. The results presented here reveal new insight into the underlying electronic and thermodynamic properties of the F-cluster relay from CpII [FeFe]-hydrogenase. Compared to other [FeFe]-hydrogenases, CpII displays a large catalytic bias for H_2 oxidation. The unique activity of CpII provides a special case to examine if properties of the FeS cluster relay are tuned to contribute to the overall efficiency of the reaction. Detailed analysis of the multifrequency EPR spectra and signal relaxation properties made it possible to resolve the individual F-cluster EPR signatures and established the presence of magnetic interactions between the clusters arising from spin-spin coupling. The results further show a unique potential landscape of the relay among those characterized thus far in [FeFe]-hydrogenases. The presence of a "high-potential" F-cluster (E_m = −140 mV ± 18) along with a more negative F-cluster (E_m = −406 mV ± 12) in CpII significantly contrasts with reduction potentials of F-cluster relays in [FeFe]-hydrogenases that exemplify more neutral bias such as CpI, which are in the range of −360 to −565 mV at pH 8 (12, 70) and therefore near the H^+/H_2 couple (E_m = −473 mV at pH 8). The large difference in midpoint potential between adjacent F-clusters in CpII (∼ΔE_m = 266 mV) is reminiscent of the potential landscape observed in two [4Fe-4S] cluster containing Fdxs, such as those from *Allochromatium vinosum* (66), *Thauera aromatica* (65), and *Azotobacter vinelandii* (76). Like CpII, these Fdxs display a relatively large difference in the redox potentials between the individual [4Fe-4S] clusters. The similarities to the F-cluster relay in CpII may reflect how [FeFe]-hydrogenases have evolved internal relays that are tuned with specific type of properties to efficiently mediate directional electron transfer. Interestingly, the large difference in midpoint potential between the CpII F-clusters is also reminiscent of the prototypical FeS cluster relay found in examples of [NiFe]-hydrogenases (24, 77, 78). These enzymes likewise display large differences in midpoint potentials between adjacent clusters (discussed further below) and, as is the case for CpII, display high catalytic rates of H_2 oxidation versus H_2 production. Given that both types of hydrogenases function in H_2 uptake, it's plausible that the respective F-cluster relays evolved common properties that contribute to the catalytic efficiency and overall physiological function of the enzymes.

The observation of a coupled F-cluster relay in CpII is thought to reflect how the relay is tuned to support directional electron transfer within the thermodynamic landscape of the CpII-Fdx reaction complex. Presumably, faster electron transfer kinetics away from the H-cluster (compared to slower kinetics to the H-cluster) would complement the flow of electrons resulting from the catalytic directionality of the H_2 oxidation reaction. For other relays, such as the photosynthetic electron transport chain that functions unidirectionally during

charge separation, electronic factors have been found to contribute in part to the directionality of electron transfer (79). The observation of electronic coupling from magnetic interactions within the relay for CpII suggests this may also be an important factor for tuning directional electron flow during H_2 oxidation catalysis. In the potentiometric titration of CpII, the appearance of spin-spin coupling features are linked and concomitant with reduction of the second F-cluster ($F_{2.061}$) that relaxes significantly faster than the first F-cluster ($F_{2.058}$). The lack of a clearly defined splitting of the g_1 or g_3 features in either F-cluster signal is in contrast to other observed splitting of the g_1 features seen in EPR spectra of spin-coupled cluster systems, such as the [FeFe]-hydrogenase from *Desulfovibrio desulfuricans* (DdHydA) (69) and the two [4Fe-4S] containing Fdx from *T. aromatica* (65). This indicates that the magnetic interaction between the F-clusters in CpII is likely more complex and represents a combination of exchange and dipolar components. In this scenario, the strength of each interaction relative to each other, along with the alignment of the electronic and geometric axes of the two F-clusters, could significantly influence the spectral shape, intensity, and position of features. The lack of observed splitting features could also indicate partial reduction rather than full reduction of the entire cluster system due to the lower E_m of the $F_{2.061}$ cluster, as seen in spectra of the two [4Fe-4S] containing Fdx of *C. pasteurianum* (68).

Two free energy models for the structural arrangement of the CpII F-clusters relative to the H-cluster (proximal F-cluster, [F_p] and distal F-cluster, [F_d]) can be envisioned for supporting electron transfer to the Fdx redox partner during H_2 oxidation catalysis (Fig. 5). For these models, the observed spin-spin coupling between F-clusters is considered to be directly linked to the Marcus electronic coupling parameter, $|H_{AB}|^2$ (35–37). Model 1, which is consistent with a previous proposal by Adams (57), places the high potential cluster (E_m = −140 mV) distal to the H-cluster (Fig. 5*A*), creating a pathway where free energy and electronic coupling are synergistic for electron flow from the H-cluster to the distal cluster but consequentially includes an uphill step of ∼272 mV to Fdx. Examination of the free energy landscape visualized as

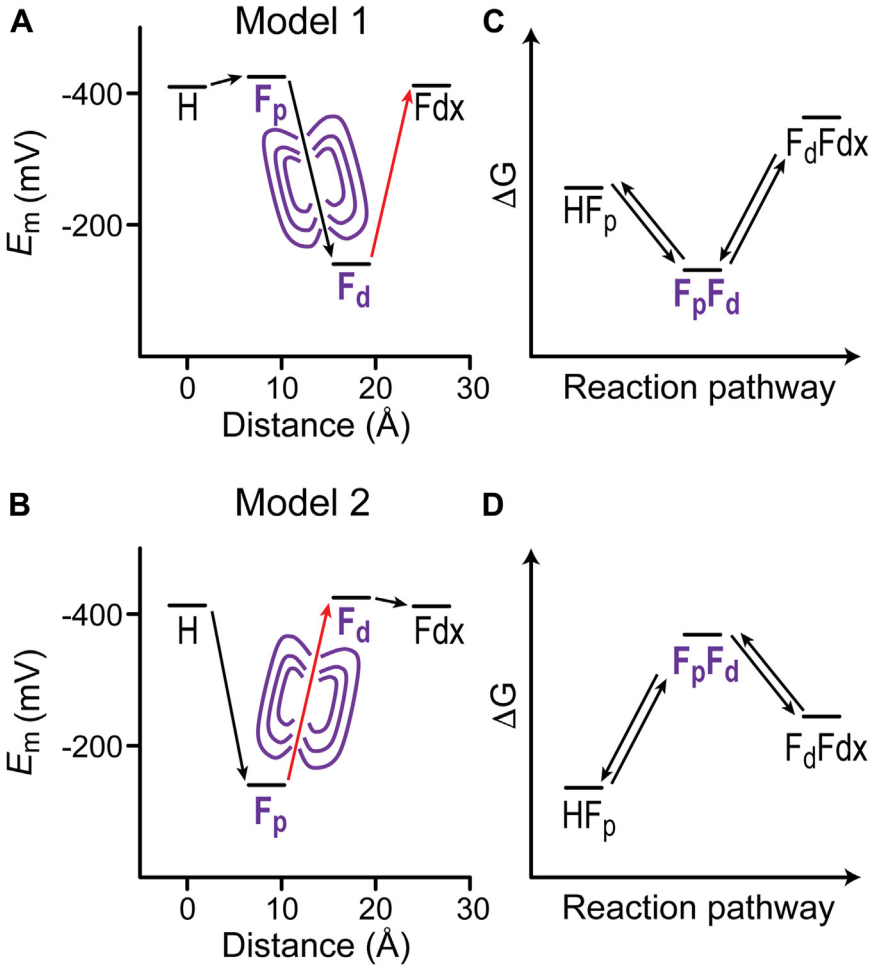

Figure 5. Landscapes for electron-flow in CpII [FeFe]-hydrogenase for the H_2 oxidizing reaction direction. *Panels A* and *B* show the reduction potential landscape of the H-cluster (H), proximal F-cluster (F_p), distal F-cluster (F_d), and ferredoxin (Fdx) redox partner for two model spatial arrangements of F_p and F_d (Model 1 and Model 2). *Red arrows* depict thermodynamic unfavorable steps. *Panels C* and *D* show the free energy profile for the individual electron transfer steps from H to F_p (HF_p), F_p to F_d (F_pF_d), and F_d to Fdx (F_dFdx) that comprise the flow of electrons from the H-cluster to Fdx during the H_2 oxidation reaction. *Purple field lines* represent coupling between F_p and F_d clusters. CpII, *Clostridium pasteurianum* [FeFe]-hydrogenase II; F_d, distal F-cluster; Fdx, ferredoxin; F_p, proximal F-cluster.

a difference in the E_m's of the clusters involved in the sequential steps—including electron transfer steps from the H-cluster to F_p (HF_p), from F_p to F_d (F_pF_d), and from F_d to Fdx (F_dFdx)—shows an overall down/up landscape with a barrier for electron flow out of the enzyme for model 1 (Fig. 5*C*). Thus, considering the previously reported high rates of H_2 oxidation activity in biochemical assays (53–55), model 1 is not favored as it would be expected to yield slow kinetics for electron transfer to Fdx.

In contrast, the arrangement in model 2 places the high potential cluster proximal to the H-cluster, creating a favorable free energy landscape for electron flow from the H-cluster to the proximal cluster (Fig. 5*B*). This arrangement creates an overall up/down landscape and a free energy barrier for electron flow from F_p to F_d that would be compensated by electronic coupling (Fig. 5*D*). The data presented here, namely spectral evidence of the spin-spin coupling between clusters, is in support of this arrangement and lends new insight as to how the interplay of coupling and thermodynamic properties of the relay can lead to fast electron transfer kinetics that support the observed high rates of H_2 oxidation activity. Interestingly, the thermodynamic landscape of model 2 is reminiscent of that found in the electron transfer chains of the *Desulfovibrio* [NiFe]-hydrogenases, where a higher in potential [3Fe-4S] cluster is arranged in between more negative in potential [4Fe-4S] clusters (77, 80, 81). For that relay, calculations by Page, Moser, Chen, and Dutton show that endergonic tunneling due to the close proximity of FeS cluster supports robust electron transfer (2). For model 2, the observed electronic coupling between the two F-clusters of CpII creates a similar scenario for endergonic tunneling within the up/down landscape and favorable electron flow to Fdx during H_2 oxidation. It's reasonable that electronic coupling between the H-cluster and F-cluster relay, which has been observed in other [FeFe]-hydrogenases such as DdHydA (82), could compound this effect and further facilitate tunneling through the free energy barrier created by the higher potential [4Fe-4S] cluster proximal to the H-cluster, thus aiding to the flow of electrons away from the H-cluster during H_2 oxidation.

Conclusions

The results of this analysis demonstrate how the properties of FeS cluster relays can be tuned to support electron transfer mechanisms that are coupled to highly biased reactions in redox catalysis. Within the model CpII [FeFe]-hydrogenase, we show that this is likely accomplished in part through a unique FeS cluster relay consisting of two spin-coupled [4Fe-4S] clusters with diverging reduction potentials. The interplay of electronic coupling and free-energy parameters of the clusters are proposed to facilitate directional electron transfer through the relay that compliments the catalytic directionality of the H_2 oxidation reaction at the active-site H-cluster. The findings signify an emerging model that suggests active sites and relays have coevolved synergistic properties which enable them to function together to achieve highly efficient catalysis. The finding that the coupling and free-energy profile of the relay act synergestically to enable efficient electron transfer to an external acceptor is likely to be a design feature found in many enzymes. For more complex FeS cluster relays found in multisubunit redox enzymes, such as those consisting of different spatial arrangements, cluster types, or relays containing a large number of clusters (26, 28, 31, 83–87), in addition to the thermodynamics, the tuning of the Marcus coupling parameter ($|H_{AB}|^2$) is thought to be an important point of control for electron reactions. This may be acheived, for example, through fine-tuning of exchange interactions between FeS clusters. For engineered systems and synthetic catalysts, designing interactions that leverage electronic coupling may lead to new strategies for controlling electron-flux and increasing the efficiencies of catalytic reactions.

Experimental procedures

Enzyme expression, purification, and biochemical assays

CpII [FeFe]-hydrogenase enzyme was expressed and purified as previously described (53). Overnight cultures were inoculated with fresh transformants and grown for 12 to 16 h at 37 °C and 250 rpm in terrific broth (TB) media (all TB media was supplemented with 0.4% glycerol). Subsequently, 5 to 10 ml of the overnight culture was then used to inoculate 1 L of TB media in a 2 L flask, and the cultures were grown to an A_{600} of approximately 0.25. Induction was carried out by the sequential addition of IPTG (1.5 mM final), cysteine (2 mM final), ferric ammonium citrate (4 mM final), fumarate (25 mM final), and glucose (0.5% final), with cultures then combined and transferred into 2 L narrow-neck flasks (Kimble Kimax) to sparge overnight with Argon gas. All subsequent steps were conducted anaerobically. Cells were harvested at 7000 rpm for 5 to 7 min, resuspended in buffer of 50 to 100 mM Tris, pH 8.3, 300 mM NaCl, 5% glycerol, and 2 mM NaDT and stored at −80 °C. Thawed cells were supplemented with protease inhibitor (EDTA-free, Roche), lysozyme, and DNAse, prior to lysing *via* 8 to 10 passes through a microfluidizer. Lysed cells were centrifuged at 45,000 rpm for 1 h and the clarified lysate passed over a preequilibrated Strep (XT-HC or XT 4-Flow) column (IBA), washed, and eluted with storage buffer supplemented with 5 mM (XT-HC) or 20 mM (XT 4Flow) biotin. Protein was stored anaerobically at 4 °C until usage. Expression and purification were verified *via* SDS-PAGE and protein concentration was determined through the Bradford assay. The specific activity of purified CpII was determined from dye-based biochemical assays measuring either H_2 production or H_2 oxidation using methyl viologen or methylene blue, respectively.

EPR sample preparation

H_2 reduced samples

H_2 reduced samples were prepared on a Schlenk line with 10 to 20 cycles of headspace exchange using 100% H_2 gas, followed by incubation for 1 to 2 h at room temperature (295 K) under an overpressure of 2 psi H_2 gas. A Schlenk line adaptor (SP Wilmad-LabGlass) allowed samples to be treated

with H_2 after being loaded into EPR tubes and samples were thus also frozen in liquid nitrogen under this overpressure.

Redox-titration samples

A steady-state equilibrium titration of CpII was performed anaerobically in an Mbraun glovebox under nitrogen atmosphere as previously reported (59). The reduction potential of the solution throughout the titration was monitored using an oxidation reduction potential electrode (Oakton 700) calibrated against a standard (Orion 967901) and adjusted for the glovebox temperature. All reported potentials were converted to be *versus* the NHE and stirring was constant throughout the titration. A redox mediator cocktail of methyl viologen, benzyl viologen, ethyl viologen, phenosafranine, indigo disulfonate, and methylene blue was prepared at 2 mM. CpII enzyme was prepared at 85 μM with any residual NaDT removed *via* buffer exchange into 50 mM Tris, 300 mM NaCl, and 5% glycerol, pH 8.3. The mediator cocktail was added to the enzyme at a final concentration of 4.5 μM and the solution potential equilibrated to −280 mV *versus* NHE. The solution was initially adjusted to positive potentials using indigo disulfonate and methylene blue, and then down in potential for all subsequent samples using NaDT. Stabilization was determined as a change of ±1 mV within a minute time period. Samples were removed from the titration cell using a Hamilton gas-tight syringe in 100 μl aliquots and immediately loaded into X-band EPR tubes with a 2.4 mm ID (Wilmad lab glass, 727-SQ-250 mm) and frozen in liquid nitrogen. The potential of the solution was carefully monitored from sample removal until actual freezing and did not deviate significantly in any case. Samples were removed at −129 mV, −197 mV, −294 mV, −397 mV, and −493 mV *versus* NHE. During titration, little to no drift in potential due to H^+ reduction was observed as the H^+/H_2 couple was reached, in line with the H_2 oxidation bias of CpII. Two buffer only control samples were prepared at the edges of the titration potential range to account for possible radical background signals from the cocktail of mediators in the ensuing analysis. Approximately the same potentials were achieved as in the −129 mV (high-potential buffer) and −493 mV (low-potential buffer) sample by using the same concentration of redox cocktail mediators and NaDT.

EPR data collection

X-band EPR (9.38 GHz)

CW EPR data were collected on a Elexsys E500 spectrometer equipped with a super high-Q resonator (Bruker), cryogen-free helium system (ColdEdge Technologies), and MercuryiTC temperature controller (Oxford Instruments). Spectra were collected at various powers and temperatures (as indicated) using a modulation frequency of 100 kHz and modulation amplitude of 10 G.

Q-band EPR (33.8 GHz)

Pulsed EPR spectra were collected on an Elexsys E580 spectrometer, equipped with a 10 W solid-state amplifier, EN5107D2 pulsed Q-band resonator (Bruker), a cryogen-free helium system (ColdEdge Technologies), and Lake Shore Cryotronics temperature controller. Electron spin echo-detected field swept spectra (referred to within this work as "pulsed Q-band spectra") were measured using the pulse sequence t_p–τ–$2t_p$–τ–echo. An initial parameter sweep was performed to identify pulsed parameters that led to the best resolution of the $F_{2.061}$ signal (Fig. S5). Based on these results, the length of the π/2 microwave pulse was set to t_p = 10 ns, with an interpulse distance of τ = 134 ns and shot repetition time of 50 to 100 μs; power was set to 0 dB of attenuation. Pseudomodulation of pulsed Q-band spectra was performed using the EasySpin function "fieldmod" with modulation of 10 G applied unless otherwise indicated.

EPR data processing

Spectra were baseline corrected as necessary by subtraction of a polynomial function in Igor Pro v.9 (https://www.wavemetrics.com/software/igor-pro-9). A binomial smoothing was applied to 0.1 mW data collected below 5 K (Fig. S3*B*). For redox titration data, the high-potential buffer collected at the same powers and temperatures was subtracted from experimental data with additional baseline correction applied in Igor Pro if necessary. At lower potentials (−395 and −493 mV samples) the low-potential buffer sample confirmed the amount of mediator background signal became more significant, although in data collected at 20 K the contribution remained low enough that it was accounted for in simulations by inclusion of a radical signal (Table S2). However, at lower temperatures this radical signal became especially prominent and overlaped with the experimental signal at $g_{2.015}$, resulting in distortion of the spectrum when subtraction was attempted and complicating the simulation approach. Therefore, the redox mediator radical is instead indicated with a dashed line in the low temperature data of these samples (Fig. 4).

Analysis of variable-temperature and variable-power CW EPR data

To obtain temperature- and power-normalized spectra of H_2 reduced CpII, variable-temperature CW data were corrected for the Curie Law through multiplication of the spectra by their respective collection temperatures (Fig. S3), while the raw EPR signal intensities (S) of variable-power data were scaled according to the relationship $S \propto \sqrt{P}$ for each spectrum (Fig. S4).

The largest Δg_n between $F_{2.061}$ and $F_{2.058}$ is at the g_2 transition (Table S2; $F_{2.061}$ g_2 = 1.92, $F_{2.058}$ g_2 = 1.931). For rhombic signals collected using CW EPR this transition is represented as a derivative feature. A typical approach to quantifying changes in signal intensity for this type of feature is to monitor the peak-to-peak amplitude, *i.e.*, a sum of the absolute intensities at the min and max derivative features, across a spectral series; however, for CpII the presence of multiple species in this spectral region complicates this type of analysis. Therefore, the temperature- and power-dependent behavior of $F_{2.058}$ and $F_{2.061}$ were assessed by monitoring the signal

intensity slightly offset the g_2 of each species, at g = 1.94 ($F_{2.058}$) and g = 1.91 ($F_{2.061}$) (Figs. S3 and S4).

For temperature data, the normalized intensities from each spectrum were plotted against the collection temperature, with a representative plot of the temperature-dependent behavior shown in Figure 2*B* for data collected at 1 mW. For power data, the normalized intensities were plotted against power in a logarithmic plot of the power-dependent behavior, shown in Fig. S4 for data collected at 3.6 K and 10 K. These data were then assessed in combination with global inspection of the spectral signatures and power-/temperature-dependent shifts to provide the T_{opt} values and optimal power (P_{opt}) ranges given in Table S1 (88, 89).

EPR simulations

Simulations were performed using the EasySpin toolbox (61) and its core function "pepper" within Matlab version R2020A (MathWorks; https://www.mathworks.com/). H_2 reduced spectra were max/min normalized prior to simulation to aid in multifrequency comparison; potentiometric data were simulated using raw intensities. The exact g-values used to simulate each spectrum are given in Table S2. Multifrequency simulation of higher temperature (Fig. S6; X-band: 21 K, Q-band: 14.4 K) data was first performed using a single component ($F_{2.058}$) and utilized a modified version of the pepper core function, "pepper_multifreq". Global simulation of the lower temperature (X-band: 10 K, Q-band: 8.8 K) multifrequency data was then performed utilizing the previously defined $F_{2.058}$ component and a second component, the $F_{2.061}$ signal (Figs. 3 and S6). For all simulations, g-value strains of [B_1 B_2 B_3] were fit and optimized for X- and Q-band data separately and are reported in Table S2. We note the consistently lower g-value strains determined for Q-band data are in line with field-independent (*i.e.*, spin-spin coupling) contributions to the spectral broadening at X-band.

As described in the results, simulation of the potentiometric data required slightly shifted g-values than those obtained from the multifrequency, 100% H_2 reduced data. These g-values were determined from global simulation of the potentiometric data at either high or low temperature. We note it is also possible the g-tensors of each species might also shift as potential changes, considering the oxidation/reduction of the paramagnetic H_{ox} state and the reduction of the second F-cluster to give the $F_{2.061}$ signal. However, given the number of parameters already being fit in the current dataset, the g-values were kept constant through the potentiometric series and g-strain was allowed to fit for each spectrum to account for any additional slight shifting of features.

Potentiometric data analysis

To assess the potential response of the $F_{2.061}$ signal and determine an approximate E_m value, the simulated contribution of $F_{2.061}$ obtained from the redox titration spectra (Fig. 4) was plotted *versus* potential. Although saturating for H_{ox} and $F_{2.058}$ species, this temperature and power maximize the signal from $F_{2.061}$ (Table S1). The use of raw data intensities for simulation allowed the simulated contribution values for each species to be compared across the potentiometric data series, and for relative changes to be assessed using the Nernst equation. While the contribution of a saturated signal would most likely be underreported with this approach, the contribution of signals collected under nonsaturating conditions should be comparable relative to one another across a series. In this manner a pseudo-Nernst curve was obtained for $F_{2.061}$ (Fig. 4, *inset*) and fit to the Nernst equation for an n = 1 process (Equation 2) using a custom fit function in Igor Pro v9 (E = potential; E_m = midpoint potential; F = Faraday constant = 96,480 C mol^{-1}; R = Gas constant 8.314 J K^{-1} mol^{-1}; T = Temperature in K) (90). The 95% confidence bands of each fit (where model points are expected to fall with a 95% or greater probability) are also shown.

$$f(E) = \frac{Maximum\ EPR\ signal}{1+e^{(E-Em)\frac{F}{RT}}} \quad (2)$$

For the $F_{2.061}$ signal, the Nernst fit was constrained to be more negative than −300 mV, based on the conclusive appearance of the signal as verified by simulation only in samples poised lower the −300 mV as well as the previously observed lack of EPR and Mössbauer signals associated with the lower potential cluster in samples poised around −300 mV (55, 56, 91).

CpII-Fdx structural complex prediction methodology

To examine possible CpII-Fdx docking interactions, the complex was predicted *via* ColabFold V 1.5.3: AlphaFold2 using MMSeqs2 (https://colab.research.google.com/github/sokrypton/ColabFold/blob/main/AlphaFold2.ipynb) (92). The following parameters were used: no template, msa_mode= mmseqs2_uniref_env, pair_mode = unpaired_paired, and advanced settings were left on default. The top five models were examined, all of which showed Fdx in a similar position relative to CpII, and the best-scored model was used for further analysis. Next, AlphaFill (93) was used to predict the FeS cluster locations in the AlphaFold CpII structure from UniProt entry R4KH70. Based on homology to CpI crystal structure 7QHF (94), the H-cluster, proximal, and distal FeS clusters were modeled into the structure. The resultant AlphaFill structure and Fdx structure 1CLF were then superimposed upon the CpII-Fdx complex that was generated *via* ColabFold.

Data availability

All data are contained within the manuscript.

Supporting information—This article contains supporting information (56).

Acknowledgments—This work was authored by the National Renewable Laboratory, operated by Alliance for Sustainable Energy, LLC, for the U.S. Department of Energy (DOE) under Contract No. DE-AC36-08GO28308. The views expressed in the article do not

Author contributions—E. C. K., J. H. A., M. B., and D. W. M. investigation; E. C. K., J. H. A., M. B., J. W. P., P. W. K., and D. W. M. writing–review and editing; E. C. K., J. H. A., and M. B. E. C. K., J. H. A., and D. W. M. data curation; E. C. K., J. H. A., and D. W. M. visualization; E. C. K. and J. H. A. validation; E. C. K., P. W. K., and D. W. M. writing–original draft; E. C. K., P. W. K., and D. W. M. conceptualization; E. C. K., P. W. K., and D. W. M. formal analysis; P. W. K. and D. W. M. funding acquisition; P. W. K. and D. W. M. project administration; P. W. K. and D. W. M. supervision.

Funding and additional information—Funding provided by the U.S. Department of Energy Office of Basic Energy Sciences, Division of Chemical Sciences, Geosciences, and Biosciences, Photosynthetic Systems Program. J. W. P. was supported by the National Institutes of Health (1R01GM138592-01). The content is solely the responsibility of the authors and does not necessarily represent the official views of the National Institutes of Health.

Conflict of interest—The authors declare that they have no conflicts of interest with the contents of this article.

Abbreviations—The abbreviations used are: CpII, *Clostridium pasteurianum* [FeFe]-hydrogenase II; EPR, electron paramagnetic resonance; $F_{2.058}$, F-cluster signal designated at g = 2.058, 1.931, 1.891; $F_{2.061}$, F-cluster signal designated at g = 2.061, 1.920, 1.887; F_d, distal F-cluster; F_p, proximal F-cluster; Fdx, ferredoxin; FeS, iron-sulfur; $|H_{AB}|^2$, electronic coupling parameter; NaDT, sodium dithionite; NHE, normal hydrogen electrode; P_{opt}, power optimum; SAM, *S*-adenosylmethionine; T_{opt}, temperature optimum; TB, terrific broth.

References

1. Winkler, J. R., and Gray, H. B. (2014) Electron flow through metalloproteins. *Chem. Rev.* **114**, 3369–3380
2. Page, C. C., Moser, C. C., Chen, X., and Dutton, P. L. (1999) Natural engineering principles of electron tunnelling in biological oxidation-reduction. *Nature* **402**, 47–52
3. Liu, J., Chakraborty, S., Hosseinzadeh, P., Yu, Y., Tian, S., Petrik, I., *et al.* (2014) Metalloproteins containing cytochrome, iron-sulfur, or copper redox centers. *Chem. Rev.* **114**, 4366–4469
4. Beinert, H., Holm, R. H., and Münck, E. (1997) Iron-sulfur clusters: nature's modular, multipurpose structures. *Science* **277**, 653–659
5. Johnson, D. C., Dean, D. R., Smith, A. D., and Johnson, M. K. (2005) Structure, function, and formation of biological iron-sulfur clusters. *Annu. Rev. Biochem.* **74**, 247–281
6. Rees, D. C., and Howard, J. B. (2003) The interface between the biological and inorganic worlds: iron-sulfur metalloclusters. *Science* **300**, 929–931
7. Frey, P. A., Hegeman, A. D., and Ruzicka, F. J. (2008) The radical SAM superfamily. *Crit. Rev. Biochem. Mol. Biol.* **43**, 63–88
8. Broderick, J. B., Duffus, B. R., Duschene, K. S., and Shepard, E. M. (2014) Radical S-adenosylmethionine enzymes. *Chem. Rev.* **114**, 4229–4317
9. Nicolet, Y. (2020) Structure–function relationships of radical SAM enzymes. *Nat. Catal.* **3**, 337–350
10. Hosseinzadeh, P., and Lu, Y. (2016) Design and fine-tuning redox potentials of metalloproteins involved in electron transfer in bioenergetics. *Biochim. Biophys. Acta* **1857**, 557–581
11. Rodriguez-Macia, P., Kertess, L., Burnik, J., Birrell, J. A., Hofmann, E., Lubitz, W., *et al.* (2018) His-ligation to the [4Fe–4S] subcluster tunes the catalytic bias of [FeFe] hydrogenase. *J. Am. Chem. Soc.* **141**, 472–481
12. Lubner, C. E., Artz, J. H., Mulder, D. W., Oza, A., Ward, R. J., Williams, S. G., *et al.* (2022) A site-differentiated [4Fe–4S] cluster controls electron transfer reactivity of *Clostridium acetobutylicum* [FeFe]-hydrogenase I. *Chem. Sci.* **13**, 4581–4588
13. Dementin, S., Belle, V., Bertrand, P., Guigliarelli, B., Adryanczyk-Perrier, G., De Lacey, A. L., *et al.* (2006) Changing the ligation of the distal [4Fe4S] cluster in NiFe hydrogenase impairs inter- and intramolecular electron transfers. *J. Am. Chem. Soc.* **128**, 5209–5218
14. Skeel, B. A., and Suess, D. L. (2023) Exploiting molecular symmetry to quantitatively map the excited-state landscape of iron-sulfur clusters. *J. Am. Chem. Soc.* **145**, 10376–10395
15. Stephens, P., Jollie, D., and Warshel, A. (1996) Protein control of redox potentials of iron-sulfur proteins. *Chem. Rev.* **96**, 2491–2514
16. Gaughan, S. J., Hirst, J. D., Croft, A. K., and Jager, C. M. (2022) Effect of oriented electric fields on biologically relevant iron-sulfur clusters: tuning redox reactivity for catalysis. *J. Chem. Inf. Model.* **62**, 591–601
17. Birrell, J. A., Laurich, C., Reijerse, E. J., Ogata, H., and Lubitz, W. (2016) Importance of hydrogen bonding in fine tuning the [2Fe-2S] cluster redox potential of HydC from *Thermotoga maritima*. *Biochemistry* **55**, 4344–4355
18. Dey, A., Jenney, F. E., Jr., Adams, M. W., Babini, E., Takahashi, Y., Fukuyama, K., *et al.* (2007) Solvent tuning of electrochemical potentials in the active sites of HiPIP versus ferredoxin. *Science* **318**, 1464–1468
19. Ohnishi, T. (1998) Iron-sulfur clusters/semiquinones in complex I. *Biochim. Biophys. Acta* **1364**, 186–206
20. Pandelia, M.-E., Nitschke, W., Infossi, P., Giudici-Orticoni, M.-T., Bill, E., and Lubitz, W. (2011) Characterization of a unique [FeS] cluster in the electron transfer chain of the oxygen tolerant [NiFe] hydrogenase from *Aquifex aeolicus*. *Proc. Natl. Acad. Sci. U. S. A.* **108**, 6097–6102
21. Jeuken, L. J., Jones, A. K., Chapman, S. K., Cecchini, G., and Armstrong, F. A. (2002) Electron-transfer mechanisms through biological redox chains in multicenter enzymes. *J. Am. Chem. Soc.* **124**, 5702–5713
22. Parey, K., Wirth, C., Vonck, J., and Zickermann, V. (2020) Respiratory complex I-structure, mechanism and evolution. *Curr. Opin. Struct. Biol.* **63**, 1–9
23. Richardson, K. H., Wright, J. J., Šimėnas, M., Thiemann, J., Esteves, A. M., McGuire, G., *et al.* (2021) Functional basis of electron transport within photosynthetic complex I. *Nat. Commun.* **12**, 5387
24. Volbeda, A., Charon, M. H., Piras, C., Hatchikian, E. C., Frey, M., and Fontecilla-Camps, J. C. (1995) Crystal structure of the nickel-iron hydrogenase from *Desulfovibrio gigas*. *Nature* **373**, 580–587
25. Shomura, Y., Taketa, M., Nakashima, H., Tai, H., Nakagawa, H., Ikeda, Y., *et al.* (2017) Structural basis of the redox switches in the NAD+-reducing soluble [NiFe]-hydrogenase. *Science* **357**, 928–932
26. Feng, X., Schut, G. J., Haja, D. K., Adams, M. W., and Li, H. (2022) Structure and electron transfer pathways of an electron-bifurcating NiFe-hydrogenase. *Sci. Adv.* **8**, eabm7546
27. Peters, J. W., Lanzilotta, W. N., Lemon, B. J., and Seefeldt, L. C. (1998) X-ray crystal structure of the Fe-only hydrogenase (CpI) from *Clostridium pasteurianum* to 1.8 angstrom resolution. *Science* **282**, 1853–1858
28. Furlan, C., Chongdar, N., Gupta, P., Lubitz, W., Ogata, H., Blaza, J. N., *et al.* (2022) Structural insight on the mechanism of an electron-bifurcating [FeFe] hydrogenase. *Elife* **11**, e79361
29. Nicolet, Y., Piras, C., Legrand, P., Hatchikian, C. E., and Fontecilla-Camps, J. C. (1999) *Desulfovibrio desulfuricans* iron hydrogenase: the structure shows unusual coordination to an active site Fe binuclear center. *Structure* **7**, 13–23
30. Dobbek, H., Svetlitchnyi, V., Gremer, L., Huber, R., and Meyer, O. (2001) Crystal structure of a carbon monoxide dehydrogenase reveals a [Ni-4Fe-5S] cluster. *Science* **293**, 1281–1285
31. Radon, C., Mittelstädt, G., Duffus, B. R., Bürger, J., Hartmann, T., Mielke, T., *et al.* (2020) Cryo-EM structures reveal intricate Fe-S cluster arrangement and charging in *Rhodobacter capsulatus* formate dehydrogenase. *Nat. Commun.* **11**, 1912

32. Peters, J. W., Stowell, M. H., Soltis, S. M., Finnegan, M. G., Johnson, M. K., and Rees, D. C. (1997) Redox-dependent structural changes in the nitrogenase P-cluster. *Biochemistry* **36**, 1181–1187
33. Paquete, C. M., and Louro, R. O. (2014) Unveiling the details of electron transfer in multicenter redox proteins. *Acc. Chem. Res.* **47**, 56–65
34. Moser, C. C., Page, C. C., Farid, R., and Dutton, P. L. (1995) Biological electron transfer. *J. Bioenerg. Biomembr.* **27**, 263–274
35. Mulder, D. W., Peters, J. W., and Raugei, S. (2021) Catalytic bias in oxidation-reduction catalysis. *Chem. Commun. (Camb)* **57**, 713–720
36. Fourmond, V., Plumeré, N., and Léger, C. (2021) Reversible catalysis. *Nat. Rev. Chem.* **5**, 348–360
37. Armstrong, F. A., Cheng, B., Herold, R. A., Megarity, C. F., and Siritanaratkul, B. (2022) From protein film electrochemistry to nanoconfined enzyme cascades and the electrochemical leaf. *Chem. Rev.* **123**, 5421–5458
38. Marcus, R. A. (1956) On the theory of oxidation-reduction reactions involving electron transfer. I. *J. Chem. Phys.* **24**, 966–978
39. Marcus, R. A., and Sutin, N. (1985) Electron transfers in chemistry and biology. *Biochim. Biophys. Acta* **811**, 265–322
40. Hayashi, T., and Stuchebrukhov, A. A. (2010) Electron tunneling in respiratory complex I. *Proc. Natl. Acad. Sci. U. S. A.* **107**, 19157–19162
41. Lukas, A. S., Bushard, P. J., Weiss, E. A., and Wasielewski, M. R. (2003) Mapping the influence of molecular structure on rates of electron transfer using direct measurements of the electron Spin– spin exchange interaction. *J. Am. Chem. Soc.* **125**, 3921–3930
42. Goodman, G., and Leigh Jr, J. S. (1985) Distance between the electron paramagnetic resonance-visible copper and cytochrome a in bovine heart cytochrome oxidase. *Biochemistry* **24**, 2310–2317
43. Gray, H. B., and Winkler, J. R. (2003) Electron tunneling through proteins. *Q. Rev. Biophys.* **36**, 341–372
44. Blumberger, J. (2015) Recent advances in the theory and molecular simulation of biological electron transfer reactions. *Chem. Rev.* **115**, 11191–11238
45. Beratan, D. N., Onuchic, J. N., and Hopfield, J. (1987) Electron tunneling through covalent and noncovalent pathways in proteins. *J. Chem. Phys.* **86**, 4488–4498
46. Peters, J. W., Schut, G. J., Boyd, E. S., Mulder, D. W., Shepard, E. M., Broderick, J. B., *et al.* (2015) [FeFe]- and [NiFe]-hydrogenase diversity, mechanism, and maturation. *Biochim. Biophys. Acta* **1853**, 1350–1369
47. Mulder, D. W., Shepard, E. M., Meuser, J. E., Joshi, N., King, P. W., Posewitz, M. C., *et al.* (2011) Insights into [FeFe]-hydrogenase structure, mechanism, and maturation. *Structure* **19**, 1038–1052
48. Meyer, J. (2008) Iron-sulfur protein folds, iron-sulfur chemistry, and evolution. *J. Biol. Inorg. Chem.* **13**, 157–170
49. King, P. W., Posewitz, M. C., Ghirardi, M. L., and Seibert, M. (2006) Functional studies of [FeFe] hydrogenase maturation in an *Escherichia coli* biosynthetic system. *J. Bacteriol.* **188**, 2163–2172
50. Gauquelin, C., Baffert, C., Richaud, P., Kamionka, E., Etienne, E., Guieysse, D., *et al.* (2018) Roles of the F-domain in [FeFe] hydrogenase. *Biochim. Biophys. Acta Bioenerg.* **1859**, 69–77
51. Caserta, G., Papini, C., Adamska-Venkatesh, A., Pecqueur, L., Sommer, C., Reijerse, E., *et al.* (2018) Engineering an [FeFe]-Hydrogenase: do accessory clusters influence O2 resistance and catalytic bias? *J. Am. Chem. Soc.* **140**, 5516–5526
52. Therien, J. B., Artz, J. H., Poudel, S., Hamilton, T. L., Liu, Z., Noone, S. M., *et al.* (2017) The physiological functions and structural determinants of catalytic bias in the [FeFe]-hydrogenases CpI and CpII of *Clostridium pasteurianum* strain w5. *Front. Microbiol.* **8**, 1305
53. Artz, J. H., Zadvornyy, O. A., Mulder, D. W., Keable, S. M., Cohen, A. E., Ratzloff, M. W., *et al.* (2020) Tuning catalytic bias of hydrogen gas producing hydrogenases. *J. Am. Chem. Soc.* **142**, 1227–1235
54. Adams, M. W., and Mortenson, L. E. (1984) The physical and catalytic properties of hydrogenase II of Clostridium pasteurianum. A comparison with hydrogenase I. *J. Biol. Chem.* **259**, 7045–7055
55. Adams, M. W. W. (1990) The structure and mechanism of iron-hydrogenases. *Biochim. Biophys. Acta* **1020**, 115–145
56. Adams, M. W. (1987) The mechanisms of H2 activation and CO binding by hydrogenase I and hydrogenase II of *Clostridium pasteurianum*. *J. Biol. Chem.* **262**, 15054–15061
57. Adams, M. W., Eccleston, E., and Howard, J. B. (1989) Iron-sulfur clusters of hydrogenase I and hydrogenase II of *Clostridium pasteurianum*. *Proc. Natl. Acad. Sci. U. S. A.* **86**, 4932–4936
58. Prince, R. C., and Adams, M. (1987) Oxidation-reduction properties of the two Fe4S4 clusters in *Clostridium pasteurianum* ferredoxin. *J. Biol. Chem.* **262**, 5125–5128
59. Mulder, D. W., Guo, Y., Ratzloff, M. W., and King, P. W. (2017) Identification of a catalytic iron-hydride at the H-cluster of [FeFe]-hydrogenase. *J. Am. Chem. Soc.* **139**, 83–86
60. Lorent, C., Katz, S., Duan, J., Kulka, C. J., Caserta, G., Teutloff, C., *et al.* (2020) Shedding light on proton and electron dynamics in [FeFe] hydrogenases. *J. Am. Chem. Soc.* **142**, 5493–5497
61. Stoll, S., and Schweiger, A. (2006) EasySpin, a comprehensive software package for spectral simulation and analysis in EPR. *J. Magn. Reson.* **178**, 42–55
62. Stoll, S., and Goldfarb, D. (2018) *EPR Spectroscopy: Fundamentals and Methods*, John Wiley & Sons, Chichester, UK
63. Hagen, W. R. (2008) *Biomolecular EPR Spectroscopy*, CRC press, Boca Raton, FL
64. Grande, H. J., Dunham, W. R., Averill, B., Van Dijk, C., and Sands, R. H. (1983) Electron paramagnetic resonance and other properties of hydrogenases isolated from *Desulfovibrio vulgaris* (strain Hildenborough) and *Megasphaera elsdenii*. *Eur. J. Biochem.* **136**, 201–207
65. Boll, M., Fuchs, G., Tilley, G., Armstrong, F. A., and Lowe, D. J. (2000) Unusual spectroscopic and electrochemical properties of the 2 [4Fe-4S] ferredoxin of *Thauera aromatica*. *Biochemistry* **39**, 4929–4938
66. Kyritsis, P., Kümmerle, R., Huber, J. G., Gaillard, J., Guigliarelli, B., Popescu, C., *et al.* (1999) Unusual NMR, EPR, and Mössbauer properties of *Chromatium vinosum* 2 [4Fe-4S] ferredoxin. *Biochemistry* **38**, 6335–6345
67. Guerrini, O., Burlat, B., Léger, C., Guigliarelli, B., Soucaille, P., and Girbal, L. (2008) Characterization of two 2 [4Fe4S] ferredoxins from *Clostridium acetobutylicum*. *Curr. Microbiol.* **56**, 261–267
68. Mathews, R., Charlton, S., Sands, R. H., and Palmer, G. (1974) On the nature of the spin coupling between the iron-sulfur clusters in the eight-iron ferredoxins. *J. Biol. Chem.* **249**, 4326–4328
69. Birrell, J. A., Wrede, K., Pawlak, K., Rodriguez-Maciá, P., Rüdiger, O., Reijerse, E. J., *et al.* (2016) Artificial maturation of the highly active heterodimeric [FeFe] hydrogenase from *Desulfovibrio desulfuricans* ATCC 7757. *Isr. J. Chem.* **56**, 852–863
70. Artz, J. H., Mulder, D. W., Ratzloff, M. W., Lubner, C. E., Zadvornyy, O. A., LeVan, A. X., *et al.* (2017) Reduction potentials of [FeFe]-hydrogenase accessory iron–sulfur clusters provide insights into the energetics of proton reduction catalysis. *J. Am. Chem. Soc.* **139**, 9544–9550
71. Dole, F., Medina, M., More, C., Cammack, R., Bertrand, P., and Guigliarelli, B. (1996) Spin-spin interactions between the Ni Site and the [4Fe-4S] centers as a probe of light-induced structural changes in active *Desulfovibrio gigas* hydrogenase. *Biochemistry* **35**, 16399–16406
72. Patil, D. S., Moura, J. J., He, S. H., Teixeira, M., Prickril, B. C., DerVartanian, D. V., *et al.* (1988) EPR-detectable redox centers of the periplasmic hydrogenase from *Desulfovibrio vulgaris*. *J. Biol. Chem.* **263**, 18732–18738
73. Lakshmi, K., Jung, Y.-S., Golbeck, J. H., and Brudvig, G. W. (1999) Location of the iron-sulfur clusters FA and FB in photosystem I: an electron paramagnetic resonance study of spin relaxation enhancement of P700+. *Biochemistry* **38**, 13210–13215
74. Vassiliev, I. R., Antonkine, M. L., and Golbeck, J. H. (2001) Iron–sulfur clusters in type I reaction centers. *Biochim. Biophys. Acta* **1507**, 139–160
75. Evans, M., Reeves, S., and Cammack, R. (1974) Determination of the oxidation-reduction potential of the bound iron-sulphur proteins of the primary electron acceptor complex of photosystem I in spinach chloroplasts. *FEBS Lett.* **49**, 111–114
76. Gao-Sheridan, H. S., Pershad, H. R., Armstrong, F. A., and Burgess, B. K. (1998) Discovery of a novel ferredoxin from Azotobacter vinelandii

containing two [4Fe-4S] clusters with widely differing and very negative reduction potentials. *J. Biol. Chem.* **273**, 5514–5519
77. Teixeira, M., Moura, I., Xavier, A., Moura, J., LeGall, J., DerVartanian, D., *et al.* (1989) Redox intermediates of *Desulfovibrio gigas* [NiFe] hydrogenase generated under hydrogen: Mössbauer and EPR characterization of the metal centers. *J. Biol. Chem.* **264**, 16435–16450
78. Greening, C., Biswas, A., Carere, C. R., Jackson, C. J., Taylor, M. C., Stott, M. B., *et al.* (2016) Genomic and metagenomic surveys of hydrogenase distribution indicate H2 is a widely utilised energy source for microbial growth and survival. *ISME J.* **10**, 761–777
79. Kirmaier, C., Bautista, J. A., Laible, P. D., Hanson, D. K., and Holten, D. (2005) Probing the contribution of electronic coupling to the directionality of electron transfer in photosynthetic reaction centers. *J. Phys. Chem. B* **109**, 24160–24172
80. Asso, M., Guigliarelli, B., Yagi, T., and Bertrand, P. (1992) EPR and redox properties of *Desulfovibrio vulgaris* Miyazaki hydrogenase: comparison with the NiFe enzyme from *Desulfovibrio gigas*. *Biochim. Biophys. Acta* **1122**, 50–56
81. Rousset, M., Montet, Y., Guigliarelli, B., Forget, N., Asso, M., Bertrand, P., *et al.* (1998) [3Fe-4S] to [4Fe-4S] cluster conversion in *Desulfovibrio fructosovorans* [NiFe] hydrogenase by site-directed mutagenesis. *Proc. Natl. Acad. Sci. U. S. A.* **95**, 11625–11630
82. Rodriguez-Macia, P., Pawlak, K., Rudiger, O., Reijerse, E. J., Lubitz, W., and Birrell, J. A. (2017) Intercluster redox coupling influences protonation at the H-cluster in [FeFe] hydrogenases. *J. Am. Chem. Soc.* **139**, 15122–15134
83. Wagner, T., Koch, J., Ermler, U., and Shima, S. (2017) Methanogenic heterodisulfide reductase (HdrABC-MvhAGD) uses two noncubane [4Fe-4S] clusters for reduction. *Science* **357**, 699–703
84. Kumar, A., Kremp, F., Roth, J., Freibert, S. A., Müller, V., and Schuller, J. M. (2023) Molecular architecture and electron transfer pathway of the Stn family transhydrogenase. *Nat. Commun.* **14**, 5484
85. Demmer, J. K., Huang, H., Wang, S., Demmer, U., Thauer, R. K., and Ermler, U. (2015) Insights into flavin-based electron bifurcation via the NADH-dependent reduced ferredoxin: NADP oxidoreductase structure. *J. Biol. Chem.* **290**, 21985–21995
86. Feng, X., Schut, G. J., Lipscomb, G. L., Li, H., and Adams, M. W. (2021) Cryoelectron microscopy structure and mechanism of the membrane-associated electron-bifurcating flavoprotein Fix/EtfABCX. *Proc. Natl. Acad. Sci. U. S. A.* **118**, e2016978118
87. Kayastha, K., Katsyv, A., Himmrich, C., Welsch, S., Schuller, J. M., Ermler, U., *et al.* (2022) Structure-based electron-confurcation mechanism of the Ldh-EtfAB complex. *Elife* **11**, e77095
88. Eaton, G. R., Eaton, S. S., Barr, D. P., and Weber, R. T. (2010) *Quantitative EPR*, Springer-Verlag/Wien, Berlin, Germany
89. Hagen, W. R. (2018) EPR spectroscopy of complex biological iron-sulfur systems. *J. Biol. Inorg. Chem.* **23**, 623–634
90. Hagedoorn, P.-L., van der Weel, L., and Hagen, W. R. (2014) EPR monitored redox titration of the cofactors of *Saccharomyces cerevisiae* Nar1. *J. Vis. Exp.* , e51611. https://doi.org/10.3791/51611
91. Zambrano, I. C., Kowal, A. T., Mortenson, L. E., Adams, M. W. W., and Johnson, M. K. (1989) Magnetic circular dichroism and electron paramagnetic resonance studies of hydrogenase I and hydrogenase II from *Clostridium pasteurianum*. *J. Biol. Chem.* **264**, 20974–20983
92. Mirdita, M., Schütze, K., Moriwaki, Y., Heo, L., Ovchinnikov, S., and Steinegger, M. (2022) ColabFold: making protein folding accessible to all. *Nat. Methods* **19**, 679–682
93. Hekkelman, M. L., de Vries, I., Joosten, R. P., and Perrakis, A. (2023) AlphaFill: enriching AlphaFold models with ligands and cofactors. *Nat. Methods* **20**, 205–213
94. Brocks, C., Das, C. K., Duan, J., Yadav, S., Apfel, U. P., Ghosh, S., *et al.* (2023) A dynamic water channel affects O2 stability in [FeFe]-hydrogenases. *ChemSusChem* **17**, e202301365